ACS OMEGA

http://pubs.acs.org/journal/acsodf

Article

Enhancing Freeze–Thaw Resistance of Alkali-Activated Slag by Metakaolin

Yongheng Zhang, Yan He,* Xuemin Cui, and Leping Liu

Cite This: *ACS Omega* 2023, 8, 20869–20880

Read Online

ACCESS | Metrics & More | Article Recommendations

ABSTRACT: Incorporating metakaolin (MK) into slag to prepare alkali-activated materials can reduce shrinkage and improve the durability of alkali-activated slag (AAS). But its durability under freeze–thaw conditions is unknown. In this paper, the effects of MK content on the freeze–thaw properties of AAS were investigated from the perspective of gel composition and pore solution. The experimental results showed that the addition of MK generates a gel mixture of C–A–S–H and N–A–S–H with a cross-linked structure and decreases the content of bound water and pore water absorption. With the increase of alkali dosage, water absorption decreased to 0.28% and then increased to 0.97%, and the leaching rate of ions was Ca^{2+} > Al^{3+} > Na^{+} > OH^{-}. When the alkali dosage was 8 wt % and the MK content was 30 wt %, the compressive strength loss rate of AAS was 0.58% and the mass loss rate was 0.25% after 50 freeze–thaw cycles.

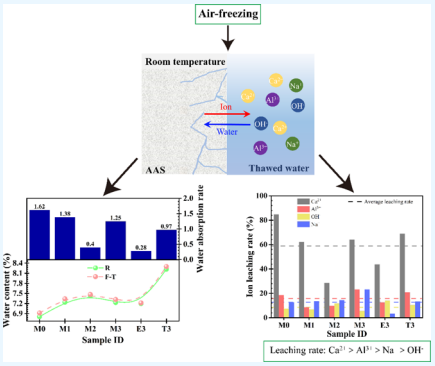

1. INTRODUCTION

In the cold regions of northern China, roads, bridges, and buildings are subjected to freeze–thaw (F–T) conditions for most of the year,[1,2] damaged by expansion of ice-forming free water in the pores. As one of the most commonly used building materials, cement concrete has more internal pore structure, which makes its capillary water absorption coefficient larger and water content increased, and its application in cold regions is vulnerable to F–T cycle damage, shortening the service life.[3−5] Therefore, the search for an environmentally friendly and durable alternative material is a necessary prerequisite for the development of the cement industry. Among them, alkali-activated materials (AAMs) are a new type of green cementitious materials with good durability performance. Moreover, AAMs have small pores and a dense structure,[6−10] which has a greater potential for application in cold regions.

As precursors commonly used in AAMs, blast furnace slag (BFS) is a calcium-rich material whose alkaline activation production, C–A–S–H gel, is similar in composition to Portland cement paste (C–S–H gel-like structure).[11] Metakaolin (MK) is a low-calcium material, and its alkaline activation produces N–A–S–H type gels.[11] The addition of MK to alkali-activated slag (AAS) can overcome the disadvantage of excessive shrinkage during early solidification and hardening of AAS[12] and also improve its corrosion resistance at a later stage.[13] Borges[14] investigated the effect of alkali-activators with different SiO_2/Na_2O molar ratios on the porosity, pore-size distribution, and durability properties of MK and BFS blended mortars. Lower SiO_2/Na_2O molar ratios promoted the reaction between MK and BFS to form a more homogeneous matrix consisting of N–A–S–H and C–A–S–H. Bernal[15] found that the carbonation rate of these materials decreased with the addition of MK and the increase of alkali-activator concentration in alkali-activated BFS/MK blended materials. Water permeability was significantly reduced under prolonged CO_2 exposure. Li and Nedeljković[12] found that with 9.3 wt % alkali dosages, the addition of MK hindered the self-shrinkage and pore-structure refinement of AAS paste. In conclusion, AAS mixed with MK can effectively reduce its autogenous shrinkage performance, improve the resistance to carbonization, and corrosion. The application of alkali-activated BFS/MK under F–T conditions has not been studied.

F–T damage is one of the major factors affecting the performance of concrete structures,[1,2] threatening their durability and safety. Zhao[16] investigated the influences of curing time (14, 28 d) and curing temperature (23, 50, 80 °C) on the F–T durability of alkali-activated red mud/fly ash blended materials based on 50 F–T cycles. In the early stage of the F–T cycle treatment, there was an obvious further polymerization and formation of a microstructure/gel. However, the geopolymer gel was partially dissolved in the

Received: March 9, 2023
Accepted: May 25, 2023
Published: June 5, 2023

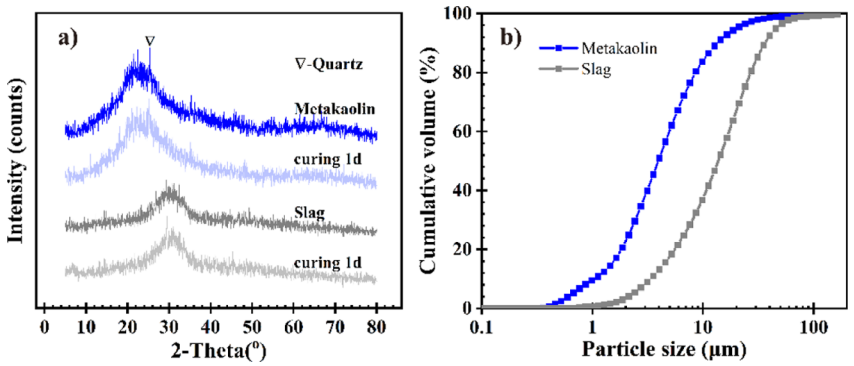

Figure 1. XRD patterns (a) of MK, BFS, and their curing 1 d and particle-size distribution (b) of MK and BFS.

Table 1. Chemical Composition of BFS, MK, and Aggregate (wt %)

oxides	SiO_2	Al_2O_3	CaO	SO_3	K_2O	NaO_2	MgO	Fe_2O_3	LOI
BFS	19.24	9.45	57.36	5.00	0.47	0.27	3.32	2.86	2.03
MK	48.75	42.34	0.11		0.09	0.39	0.13	0.48	7.71
aggregate	98.42	0.67	0.18	0.03	0.29	0.05	0.02	0.21	0.13

Table 2. Mix Proportions for AAS

sample ID	BFS (g)	MK (g)	MK/(BFS + MK) (wt %)	aggregate (g)	activator (g)	alkali dosages (wt %)[a]	w/s[b]	water (g)
M0	450	0	0	1350	143.51	6	0.4	128.07
M1	405	45	10	1350	143.51	6	0.4	128.07
M2	360	90	20	1350	143.51	6	0.4	128.07
M3	315	135	30	1350	143.51	6	0.4	128.07
E3	315	135	30	1350	201.06	8	0.4	107.28
T3	315	135	30	1350	264.85	10	0.4	84.21

[a]Alkali dosages: mass ratio of sodium oxide content to total solid content. [b]w/s: water−solid ratio; the water included deionized water and the water content of modified water glass; the solid represents all cementitious materials and the solid content of modified water glass.

later stages of the F−T cycles. The samples cured at 50 °C had better F−T resistance, but high temperature maintenance conditions are not conducive to the large-scale application of AAM in construction. Fu[17] used the relative dynamic elastic modulus (RDM) to establish a mechanical model of F−T damage of AAS concrete, which can be used to evaluate and predict the standard life of concrete in F−T cycles. Setzer[18] proposed a model for the growth of micro-ice crystals: at low temperatures, the large pores formed ice nuclei first, and the small pores were affected by the surface tension to form over-cooled water, resulting in a higher negative pressure, which drove the over-cooled water to move toward the ice nuclei, causing the small pores to shrink. When dissolved at elevated temperatures, the ice nuclei melted and caused the small pores to expand, increasing the water saturation and destroying the internal structure. Previous works have found that alkali-activated composites can effectively modulate F−T resistance.[16,19,20] In addition, no experimental study has been designed to analyze the linkage with F−T resistance in terms of bound-water content.

Based on the above analyses, the aim of this study is to vary the gel product of AAS by varying the MK and alkali dosages and analyze the relationship between the variation of bound water and pore solution with F−T resistance. The mechanical properties, dynamic elastic modulus, and mass loss of alkali-activated MK/BFS specimens under different F−T cycles were used to evaluate their F−T resistance. Field-emission scanning electron microscopy (SEM)−energy dispersive spectroscopy (EDS) and pore structure were used to analyze the microstructural changes so as to reveal the F−T damage mechanism, and an optimal ratio was found.

2. MATERIALS AND METHODS

2.1. Raw Materials. In this study, BFS provided by Beihai Chengde Group Company and MK provided by Inner Mongolia Chao Brand Building Materials Technology Company were used as solid precursors of alkali-activated composite cementitious materials. The specific surface areas of BFS and MK were 3.39 ± 0.31 and 15.32 ± 0.07 m^2/g, respectively. The XRD and particle-size distributions of BFS and MK are shown in Figure 1; MK contains a small amount of quartz. The particle size of MK is larger than that of BFS (Figure 1b), and both of their main compositions are amorphous structures with D_{50} of 13.78 and 3.96 μm, respectively. The XRD patterns of BFS and MK pastes cured for 1 d (in Figure 1a) show that the dispersion peaks of BFS and MK do not change significantly. This indicates the presence of numerous unreacted MK/BFS. The oxide composition of BFS and MK were determined by X-ray fluorescence. China ISO standard sand from Xiamen ISO Standard Sand Co., Ltd was used as the AAM aggregate. The chemical compositions are summarized in Table 1. Liquid water glass (WG; also known as sodium silicate solution) supplied by Zhongfa Water Glass Factory, Foshan, China, and sodium hydroxide (96 wt % purity) supplied by Sinopharm Chemical Reagent Company were used as alkali-activators. The solid content and modulus ($M = n(SiO_2)/n(Na_2O)$) of the commercial sodium silicate solution ($Na_2O(SiO_2)$ n −

https://doi.org/10.1021/acsomega.3c01600
ACS Omega 2023, 8, 20869−20880

xH_2O) were 37.3 and 2.92 wt %, respectively. Modified liquid sodium silicate (1M-WG) with module 1 was prepared. 24.61 g of sodium hydroxide (96 wt % purity) and 100 g of sodium silicate solution were mixed so that the $n(SiO_2)/n(Na_2O)$ ratio equals 1. The mixture was stirred in a beaker with a glass rod. The mixed activator solution was stored at room temperature (20 ± 1 °C) for 24 h before use. 1M-WG is not easy to cure at room temperature and has high alkalinity. Therefore, it is suitable to be used as an activator.

2.2. Mix Proportion and Preparation of Specimens. The mixture ratio of precursor, activator, and water is shown in Table 2. Based on the study of Li[12] and El Moustapha,[21] it is proposed to add MK to alkali-excited BFS in this study. Combined with the literature,[12,22−24] it is found that the appropriate range of alkali content is in the range of 4−12%; water−solid (w/s) ratio is in the range of 0.35−0.5. 6, 8, and 10% alkali dosages were studied by the control variable method, and the w/s ratio was fixed at 0.4.

2.2.1. Mortar Preparation. BFS and MK were mixed according to Table2 and stirred in a miniature concrete blender for 3 min; sand with a binder−sand mass ratio of 1:3 was taken, and an appropriate mass of standard sand was added to the blender and stirred for 5 min until the raw materials were combined homogeneously. According to the water−binder ratio (w/b) and corresponding alkali dosages in Table2, deionized water and 1M-WG were mixed with a glass rod and added to the blender with a lower speed to stir for 1 min and then stirred with a high speed for 3 min. The mixed mortar was poured into cuboid (40 × 40 × 160 mm^3) and cubic (40 × 40 × 40 mm^3) molds, vibrated using the shaking table for 2 min to remove the air, and placed in the chamber with constant temperature and humidity of 20 ± 1 °C and 90 ± 10 wt %, respectively. The mortar was demolded after 24 h of curing and continued to be maintained in the chamber at 20 ± 1 °C and 90 ± 10 wt %; the constant temperature and humidity curing chamber controls the humidity through the evaporator and condensation system.

2.2.2. Paste Preparation. The mixed paste was poured in a cube (40 × 40 × 40 mm^3) mold, and the following steps were referred to for the mortar.

2.3. F−T Cycles Test. The specimens were maintained in a constant temperature and humidity chamber at 20 ± 1 °C with a relative humidity of 90 ± 10% for 24 d. After soaking in water for 4 d, the F−T cycles experiments were conducted on the samples cured for 28 days. In each experimental group, three specimens were not subjected to F−T treatment, while the other three specimens were subjected to F−T experiments for 50 cycles with reference to CSN 72 2452 and ASTM C666. The specimens were removed after 4 d of soaking and wiped with a wet towel and placed on an F−T tray. The specimens were put into an air frozen refrigerator at −20 °C (±5 °C) for 3 h. After that, the specimens were thawed in water at room temperature for 1 h until the temperature of the specimens raised to 5 °C (±1 °C); this whole process is equivalent to 1 F−T cycle. After every 5 F−T cycles, the mass and dynamic modulus of elasticity were measured by electronic scales and dynamic modulus of elasticity instruments, respectively. The mass loss rate (ΔW_{ni}) of mortar specimens were calculated by eq 1.

$$\Delta W_{ni} = \frac{W_{0i} - W_{ni}}{W_{0i}} \times 100 \quad (1)$$

where W_{ni} and W_{0i} are the mass values of the ith specimen after n F−T cycles and before F−T cycles. The mass loss rate is used to evaluate the apparent performance of the specimen during F−T cycles. The relative dynamic modulus of elasticity (P_{ni}) is calculated by eq 2.

$$P_{ni} = \frac{f_{ni}^2}{f_{0i}^2} \times 100 \quad (2)$$

where f_{ni} and f_{0i} are the longitudinal frequencies of the ith specimen after n F−T cycles and before the F−T cycles, respectively. The calculation and measurement of dynamic modulus of elasticity were done according to SL352-2006 (test code for hydraulic concrete).[25]

2.4. Mechanical Properties Test. The specimens treated with different methods were placed at room temperature for 3 d, and then the compressive strength of the specimens was determined using the HYZ-300.10 constant loading cement flexural and compressive testing machine. At a loading rate of 2 kN/s, the compressive strength test was carried out with three tested specimens and three cubic specimens. The effective average value was taken as the compressive strength.

The strength loss rate (ΔC) of mortar specimens is calculated by formula 3, where C_R and C_{F-T} are, respectively, the average compressive strength values of the specimen before and after F−T cycle.

$$\Delta C = \frac{C_R - C_{F-T}}{C_R} \times 100 \quad (3)$$

2.5. Microstructure and Mineralogical Analysis. The pore structures of BFS/MK sample pastes were analyzed with the nitrogen adsorption technique and Barrett−Joyner−Halenda (BJH) method on a Gemini VII (Micromeritics Instrument Corporation, USA) instrument. Phase compositions were characterized on a Cu Kβ target using an X-ray diffractometer (Rigaku MiniFlex 600, RIKEN, Japan). The test conditions were 40 kV, 15 mA current, scan wavelength 0.1392 nm, scan step 0.02°, scan speed 10°/min, and scan range 5−80°. The XRD curves were analyzed with MDI Jade 6 software. Infrared spectra were obtained by a NICOLET iS10-Thermo SCIENTIFIC instrument with the wavenumbers of 400−4000 cm^{-1}. The pressed slices method was used with potassium bromide as the background. Samples were prepared by mixing 1 mg of the specimen with 100 mg of KBr, which were pressed into thin slices using a tablet press. The BFS/MK samples were ground into about 1 mm small particles and screened through a standard sieve, model GB/T6003.1-2012, dried at 120 °C for 2−3 h, and 0.1 g was taken for pore structure analysis. The thermogravimetric analyzer (TGA 2) provided by the Swiss company Mettler Toledo was used to analyze the thermal stability of the sample. The samples were ground into a powder and immersed in anhydrous ethanol for 3 d to terminate hydration, anhydrous ethanol was replaced once a day; samples were dried in an oven at 60 °C for 2 h and weighed. It was added to an aluminum crucible of size Ø6*4.5 mm with a capacity of 70 μL for measurement. The temperature was raised at 5 °C/min in a nitrogen atmosphere (50 mL/min, high-purity nitrogen) from the initial temperature of 30 °C, and the weight change information of the samples was recorded in the range of 30−1000 °C. The test was repeated twice for each sample. The specimens were analyzed by SEM and EDS using an SU8220 device (Hitachi, Ltd., Japan) at an acceleration voltage of 15 kV. The specimens were ground

https://doi.org/10.1021/acsomega.3c01600
ACS Omega 2023, 8, 20869−20880

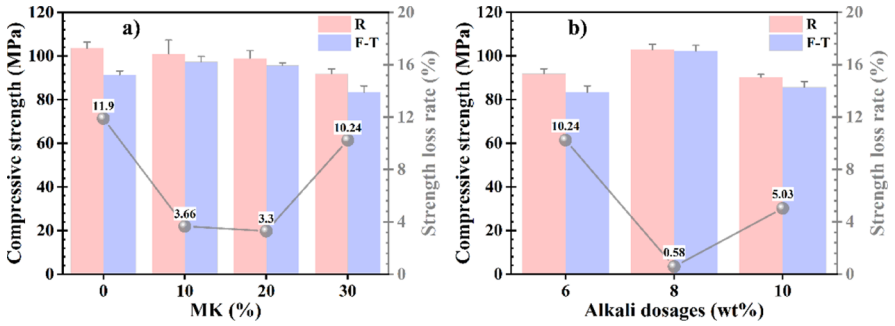

Figure 2. BFS/MK samples compressive strength before (R) and after F−T for 28 d curing (a) 6 wt % alkali dosages; (b) 30 wt % MK.

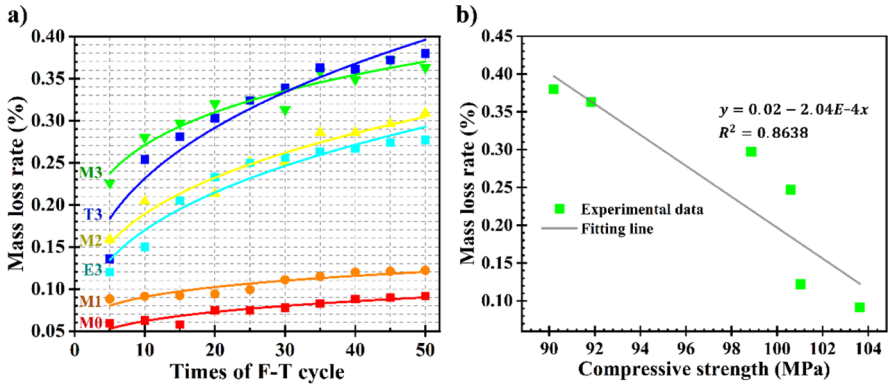

Figure 3. Mass loss rate (a) of BFS/MK samples during F−T test and (b) relationship between compressive strength and mass loss rate.

with a water mill, immersed in anhydrous ethanol, cleaned with ultrasonic instruments, and then dried at 60 °C for 4 h. The energy spectra of twelve samples were tested, and the energy spectrum of each sample was scanned at six spots to summarize the rule of element change.

2.6. Water Content and Pore Solution Analysis. Free water content was determined referring to the method used by Natkunarajah.[26] The initial weight of the specimens before and after the F−T treatment were measured, and then the samples were carefully broken into small pieces without any loss. All broken parts were dried in an oven at 105 °C until a constant weight was obtained. The free water content of the specimen was calculated using eq 4, and the calculated free water content is the amount of pore solution in the specimen.

$$\%\, m_{w105} = \frac{m_0 - m_{s105}}{m_{s105}} \times 100 \tag{4}$$

The water absorption rate ($\Delta m_{\text{water absorption}}$) of mortar specimens before and after F−T cycles is calculated by formula 5, where $m_{w105,R}$ and $m_{w105,F-T}$ are, respectively, the free water content of the specimen before and after the F−T cycle.

$$\Delta m_{\text{water absorption}} = \frac{m_{w105,F-T} - m_{w105,R}}{m_{w105,R}} \times 100 \tag{5}$$

The concentration of hydroxide was determined by the hydrochloric acid (0.1 mol/L) titration method, and standard phenolphthalein solution was used as an evaluation indicator. The gel dissolution and pore expansion were affected by OH^- leaching. The deterioration degree of the samples was analyzed by the change of OH^- concentration. First, 20 mL of deionized water (V_{dw}) and 10 g of powder (m_p) specimens (two groups were made for each sample) were mixed and stirred at 500 rpm for 30 min with a magnetic stirrer, and then the mixture was poured into centrifuge tubes and centrifuged at 8000 rpm for 15 min. 10 mL of its supernatant was taken and injected into a beaker, three drops of phenolphthalein solution were added into the beaker, and the solution turned red. Hydrochloric acid was slowly added to the beaker through the acid−base burette, the beaker was rotated continuously until the solution turned colorless. After titration, the amount of hydrochloric acid added to the beaker was recorded as V_{HCl} (mL). The concentration of OH^- ($[OH^-]$, mmol/L) was determined as

$$[OH^-] = \frac{0.1 V_{HCl}}{10} \times (V_{dw} + m_p \times m_{w105}) \times 1000 \tag{6}$$

20 mL of deionized water and 1 g of the sample powder were mixed and stirred together at 500 rpm for 5 min, then the suspension was filtered through a 50 μm filter membrane, the filter residue continued to be stirred with 10 mL of deionized water, and the filtrate from the above two filtrations was added to a 1000 mL volumetric flask at a constant volume and then placed in an ultrasonic cleaner for sonication. 20 mL of the diluted solution were taken to analyze Ca^{2+}, Al^{3+}, and Na^+ by inductively coupled plasma emission spectroscopy.

3. RESULTS AND DISCUSSION

3.1. Mechanical Properties. Figure 2 shows the evolution of compressive strength and the variation of strength loss rate of BFS/MK samples mortar with different alkali dosages and MK incorporation under room-temperature maintenance or F−T conditions. When the alkali dosage was 6 wt %, the compressive strength at room temperature decreased from 103.63 MPa (M0) to 91.83 MPa (M3) with the increase of MK incorporation. The possible reason is that the substitution of BFS by MK leads to a decrease in the solubility of Ca.[22] Its

https://doi.org/10.1021/acsomega.3c01600
ACS Omega 2023, 8, 20869−20880

Table 3. Power Function Fitting Parameters for Mass Loss Rate

	M0	M1	M2	M3	E3	T3
a	3.6262×10^{-4}	6.0306×10^{-4}	9.5756×10^{-4}	0.0017	6.8366×10^{-4}	8.6933×10^{-4}
b	0.2326	0.1766	0.2958	0.1937	0.3778	0.3975
R^2	0.8755	0.8541	0.9548	0.9362	0.9216	0.8971

compressive strength is much higher than that of cement mortar containing diatomite (<60 MPa)[27] and cement mortar (blended with BFS) with a compressive strength of 72.8 MPa.[28] The strength loss of the specimens without MK was closer to the rating index of 15% for F−T loss. The lowest was 3.3% at 20 wt % MK, and the rate of strength loss increased when the dosing amount was too high. This might be relevant to excessive MK resulting in a higher pore volume (in Figure 7).[12] The trend of strength loss illustrated that with the 6 wt % alkali dosages and 10−20 wt % MK, AAS exhibited excellent F−T resistance.

The compressive strength loss of BFS/MK samples increased to 10.24% when the content of MK was increased to 30% (see Figure 2a). The reason is that N−A−S−H and C−A−S−H gels generated by adding 30 wt % MK to the system under low alkalinity conditions were reduced. Moreover, the addition of MK leads to the formation of more oligomers of so-called "sialates"[29] and "polysialate siloxo",[30] wherein the contribution of alkaline metals from the activator holds little interaction in the structuration of the microstructure. Therefore, the alkalinity was increased appropriately to enhance the polymerization of MK for further research. It was found that when the alkali dosage was 8 wt %, with 28 days curing, the compressive strength was 102.9 MPa before F−T and the compressive strength loss was 0.58 wt % (Figure 2b). The compressive strength of the 10 wt % alkali dosages specimen was lower than those of 6 and 8 wt % and did not exceed 90 MPa. It shows that when the MK content is 30 wt %, the alkali dosage of 8 wt % is the optimal ratio.

3.2. Mass Change and Relative Dynamic Elastic Modulus. Figure 3a shows the scatter fitting diagram of mass loss, obtained from the power function eq 7 and experimental test results

$$Y = ax^b \tag{7}$$

At 6 wt % alkali dosages, the mass loss of the sample increased from 0.09 wt % (M0) and 0.12 wt % (M1) to 0.30 wt % (M2) and 0.36 wt % (M3) with the addition of MK; the a-values in the fitted functions were consistent with this trend as well (see Table 3). This indicates that MK makes the surface particles of AAS samples easy to spall. With the increase of alkali dosage, the reaction degree of sample E3 increased, and the mass loss rate was 0.27 wt % with a variation trend of 6.83×10^{-4}, which were lower compared with those of M3. The high alkali dosage in sample T3 led to alkali leach[31] and increased mass loss rate. The variation of mass loss is consistent with that of compressive strength. According to the curves obtained under linear decay function fitting in Figure 4b, it is evident that there was linear decay relationship between the mass loss rate and compressive strength; this indicates that enhancing the strength can reduce the apparent mass loss. And there was no primary correlation between mass loss and internal damage.

Figure 4 shows the scatter lines diagram of the RDM, obtained by fitting the one-dimensional function eq 8 and the experimental test results

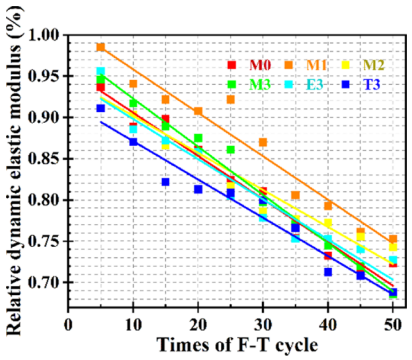

Figure 4. Relative dynamic elastic modulus of BFS/MK samples during F−T test.

$$Y = a \pm bX \tag{8}$$

The internal damage of the specimens after F−T cycles could be more visually determined. The original RDM of M1 was the highest among the specimens at 1.01%, but the trend of RDM loss for M1 was 0.0053, close to 0.0052 (M0) and similar to 0.0058 (M3), higher than 0.0045 (M2), indicating further deterioration of performance later with increasing number of F−T cycles. The variation of RDM showed that the RDM loss of M2 and E3 specimens tend to be at a lower level, in the range of 0.0045−0.0049, and the original RDM is relatively moderate, near 0.95%, and thus exhibits better resistance to F−T. The residual RDM values of M3 and T3 are 0.68 and 0.69%, respectively, The T3 specimen showed a lower deterioration trend (0.0046); this indicates that the specimens showed worse damage in the initial stage and may be related to high alkali dosages (Table 4).

Table 4. One-Dimensional Function Fitting Parameters for the Relative Dynamic Elastic Modulus

	M0	M1	M2	M3	E3	T3
a	0.9581	1.0109	0.9467	0.9813	0.9502	0.9177
b	0.0052	0.0053	0.0045	0.0058	0.0049	0.0046
R^2	0.9591	0.9476	0.9346	0.9862	0.9395	0.9542

3.3. Pore Structure Analysis. The pore-size distribution curves analyzed by BJH in Figure 5 show different pore-size distributions in the range of 1−200 nm. According to the results of the previous studies,[32,33] these pore sizes can be divided into two categories: gel pores in the range of 1−10 nm and capillary pores corresponding to the spaces left by unreacted water in the AAS paste during the polymerization process, which range from 10 to 200 nm. Capillary pores are responsible for the macroscopic mechanical properties.[34,35] The surface tension of water increases with the decrease of pore size and the freezing point of water decreases. From larger pores (10−105 nm) to gel pores (3−10 nm), the freezing temperature of water decreases from 0 to −4 to −30 to −80 °C.[36]

https://doi.org/10.1021/acsomega.3c01600
ACS Omega 2023, 8, 20869−20880

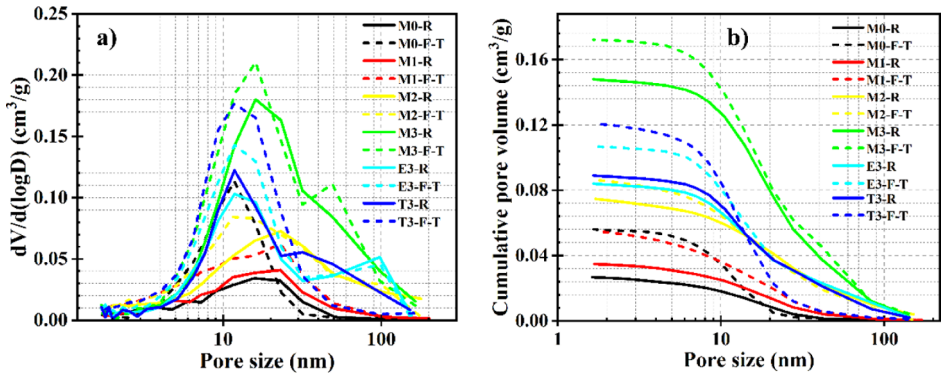

Figure 5. Pore size (a) and cumulative pore volume distribution (b) of BFS/MK samples before and after F−T test.

Figure 5a,b shows the pore-size distribution and cumulative pore volume of different AAS specimens after 50 F−T cycles. Along with the addition of MK, the specific surface area of the specimens increased from 10.013 to 28.563 m^2/g, the cumulative pore volume and the pores of 5−100 nm increased gradually, which reduced the compressive strength of the specimens.[12] After 50 F−T cycles from −20 °C (±5 °C) to 5 °C (±1 °C), the cumulative pore volume of 5−20 nm of M0 specimens increased by 0.0334 cm^3/g, which is much larger than 0.0092 cm^3/g (M1) and 0.0026 cm^3/g (M2) and more pores were ∼>10 nm. Micropores of 1−4 nm were affected by the expansion of capillary pores and led to the rupture of nearby micropores. This should be related to microcracks formation and the partial dissolution of the geopolymer gel caused by the F−T tests.[16,37]

In the pore-size distribution of M3, the excess MK causes the pores numbers in the range of 20−200 nm increased significantly. After the F−T treatment, a narrow peak appeared at 50 nm, which formed bimodal pore-size distribution with 20 nm and a larger volume of interconnected pores, resulting in the internal deterioration of the specimen. Sample E3 exhibited a bimodal pore-size distribution at 10−20 nm and 100 nm. After the F−T treatment, the peaks were shifted toward the lower pore size, which indicates that the internal structure did not deteriorate significantly. The variation of the peak area of the integrated pore in T3 corresponds to the variation of the cumulative pore volume; the cumulative pore volume increased by 0.0505 cm^3/g for those less than 30 nm and decreased by 0.0179 cm^3/g for those greater than 30 nm after the F−T treatment, which corresponds to a slowing trend of RDM deterioration in the later stage. The cumulative pore volume of sample E3 was 0.084 cm^3/g, and the cumulative pore volume increased by 0.023 cm^3/g after the F−T treatment, which was lower than that of samples M3 and T3. It indicates that when the content of MK in AAS was 30 wt % and the alkali dosage was 8 wt %, a relatively dense gel structure was easy to form and the excellent F−T resistance may be attributed to the development of polymerization of geopolymer gels during F−T cycles (Table 5).

3.4. XRD and FTIR Analysis. Figure 6a shows the XRD results of the specimens before and after the F−T treatment. The diffraction peak intensity of the crystals is related to the MK/(BFS + MK) ratio and the F−T treatment conditions. The spectral analysis shows that the peaks formed at about 6° 2Θ and 29° 2Θ correspond to the C(N)−A−S−H amorphous gel phase, and the weak peak formed at 12° 2Θ corresponds to the main reflection of hydrotalcite-type products.[38,39] A crystal

Table 5. BET Surface Area

	BET surface area (m^2/g)	
	R	F−T
M0	10.013	19.253
M1	11.164	19.215
M2	19.787	25.710
M3	28.563	35.174
E3	18.724	25.968
T3	19.604	28.373

peak of calcite is also present at about 29° 2Θ.[39] With the increase of MK incorporation, the intensity of the C−(A)−S−H gel peaks formed at about 29° 2Θ gradually decreases. It is possible that the higher content of Al_2O_3 in MK dissolves into the aluminum−oxygen tetrahedra under the activation, replacing part of the silicon−oxygen tetrahedra on the gel chain and forming N−A−S−H/C−A−S−H hybrid gels, which causes lower crystallization.[40] No new characteristic peaks appeared in the specimens after F−T treatment, it indicates that the F−T conditions had no effects on the crystalline components of the substances.

Figure 6b illustrates the FTIR spectra of AAS with different MK content in the wavenumbers ranging from 400 to 4000 cm^{-1} and the trend of the wavenumbers of stretching vibrations of Si−O−T and O−H before and after F−T cycles. The broad band at 3450 cm^{-1} in Figure 6b corresponds to the stretching vibrations of O−H groups in the weaker crystalline phase or constrained water and hydroxyl groups.[41] The resonances are typical of bound and interlayer water within the C(N)−A−S−H gels, along with crystal water within the hydrotalcite-type products, consistent with the phases observed by XRD.[39] Broad peaks in the 950−1100 cm^{-1} region are often used to characterize the Si−O−T (T = Si or Al) asymmetric stretching vibrational band in gels,[42,43] also called the "main band". The wavenumbers of the main bands of the MK-doped samples are higher than that of sample M0, which may be related to the generation of hybrid gels or the asymmetric stretching vibration of unreacted MK.[44] The XRD pattern shows that the peak intensity at 29° 2Θ becomes lower. After the F−T treatment, the main bands of samples M0 and M1 became wider, which could be related to the decalcification dissolution of C−A−S−H gels.[45] The main bands of samples M2, M3, E3, and T3 were narrowed. This is likely caused by the continuous increase of silicates or substitution of tetrahedral Al in the gel structure.[16,46] The gray dotted lines labeled non-dominant peaks in the figure at about 450, 710, 1430, and 1650 cm^{-1} correspond to O−Si−O bond bending

https://doi.org/10.1021/acsomega.3c01600
ACS Omega 2023, 8, 20869−20880

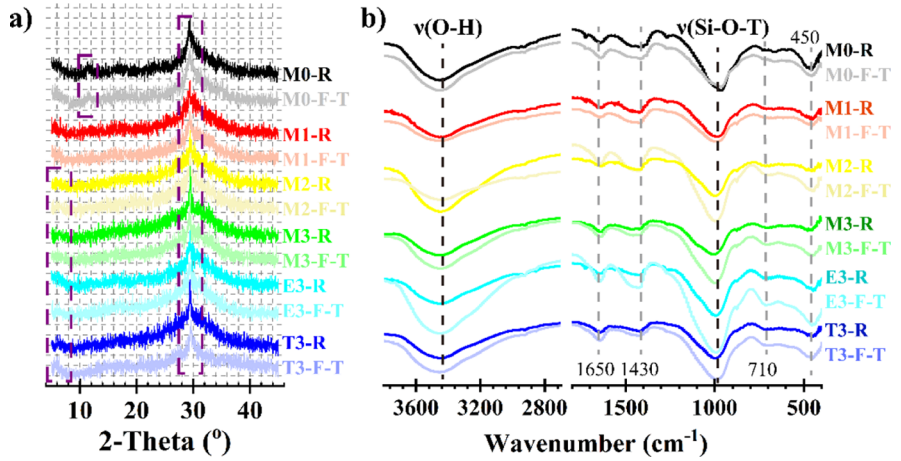

Figure 6. XRD patterns (a) and FTIR curves (b) of BFS/MK samples after F−T test.

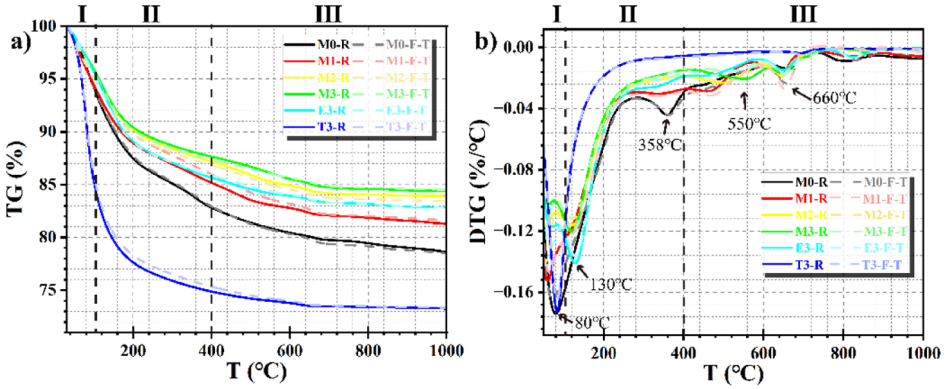

Figure 7. TG (a) and DTG (b) curves of BFS/MK samples before and after F−T test.

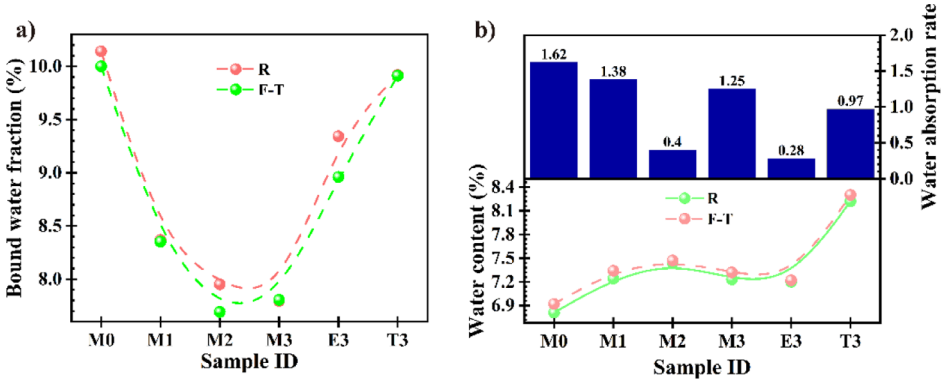

Figure 8. Bound water fraction (a) and water content and water absorption rate (b) of AAS before and after F−T test.

vibrations,[44] Si−O−Al bond bending vibrations,[47] C−O bond stretching vibrations in CO,[3−42] and O−H bending vibrations in calcium silica−aluminate hydrate,[48] respectively.

3.5. Thermogravimetric Analysis. To evaluate the mass fraction of the different phases (C(N)−A−S−H gels and $CaCO_3$, etc.) present in the BFS/MK samples, TG experiments were performed on these specimens before and after the F−T cycles. The results of the TG−derivative TG (DTG) analysis of these specimens are shown in Figure 7. The first region is the weight loss peak at 80 °C, which could be assigned to the weight loss of uncrystallized calcium alumina and free water according to a previous study.[39,49] The third region was mainly related to the decarbonation of calcium carbonate, and the amorphous or poorly crystallized calcium carbonate decarburized at about 550 to form a peak.[50] The E3 specimen showed a evident peaks at 650 and 800 °C, which should be a small amount of well-dispersed crystalline calcium carbonate.[50,51] The weak peak of sample M1 formed at 400−500 °C should be related to the decomposition of hydrotalcite products.[48,52] For M0, M1, and E3 samples with higher calcium content, the relative contents of calcium carbonate increased after F−T, mainly related to the exposure to air during the experiment.

The mass loss in the range between 150 and 500 °C is associated with the loss of bound water as a result of decomposition of C−(N)−A−S−H or other hydration

https://doi.org/10.1021/acsomega.3c01600
ACS Omega 2023, 8, 20869−20880

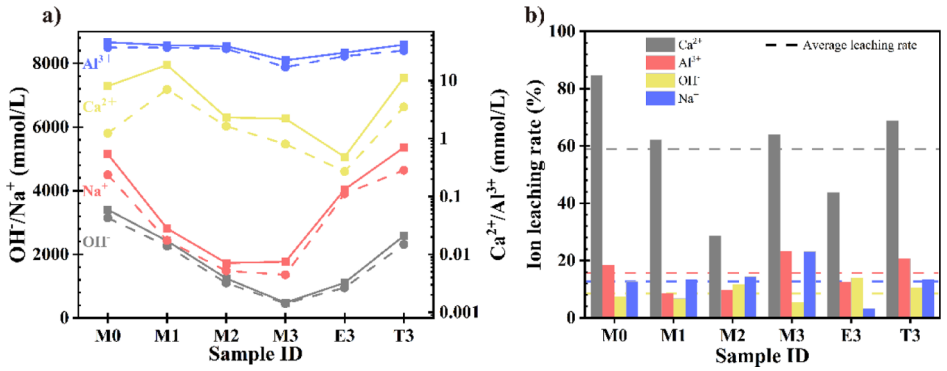

Figure 9. (a) Concentration and (b) leaching rate curves of OH^-, Ca^{2+}, Al^{3+}, and Na^+ before and after F−T treatment.

products such as hydrotalcite.[53,54] The second region shows two peaks for the weight loss. The weight loss peak at about 130 °C is attributed to the removal of bound water in C−(N)−A−S−H.[39,53] The replacement of silica−oxygen tetrahedra by aluminum−oxygen tetrahedra increased the interlayer spacing of the mixed gel products, accumulated more bound water in the individual C(N)−A−S−H spheres, and the weight loss peak became intense at about 130 °C.[48] The gel water loss peaks were similar for M0 and T3 specimens, which should be influenced by the silicon and aluminum content. The lower aluminum content of M0 generated more C−S−H gels. The higher the alkali dosage and free silicon content in T3, the more gel products and silicate oligomers were generated.[39,55] The bound water weight loss peak became weaker, and the mass loss curve shifted upward. The single peak formed of M0 at 358 °C is due to the decomposition of hydrotalcite.[48,52] Combined with refs 56 and 57, the bound water mass fraction could be calculated from the mass loss in the range of 105−400 °C (in Figure 7a).

3.6. Water Content and Pore Solution Analysis. Figure 8a shows the bound water fraction in BFS/MK samples obtained from TG. With the increase of MK content and alkali dosages, the content of bound water in the specimens varies in a "U" shaped curve. Due to the high correlation between bound water and interlayer water, the interlayer water and gel content also met this variation. After the F−T treatment, the fraction of bound water in the samples decreased relatively, this consolidated the Al−O stability in the gel and reduced the Al migration.[58] Among them, the bound water content of M2 and E3 decreased by 4.10 and 3.27 wt %, respectively. This indicates that the gel dissolved and rearranged under the F−T treatment[16] and filled the pores, resulting in the reduction of the bound water fraction. The bound water fractions of M1 and M3 appeared to be much more stable. These inconsistent variations in AAS samples indicate that the stability of bound water molecules in the N−A−S−H/C−A−S−H hybrid gels interlayer may greatly depend on the MK incorporation and alkali dosages. This will be further investigated by SEM−EDS analysis later.

In Figure 8b, the water content of the specimens increased with the increase of MK content and alkali dosage, which was related to the polymerization reaction degree of AAS. The water content increased about 0.71 wt % after the F−T treatment. This should be related to the increase of internal pore volume and connected pores. The water absorption of sample M0 is relatively high, while the water content of M2 and E3 slightly decreased due to the cross-linked structure of the internal gels, which exhibited a dense structure and less water absorption. This may further affect the free water demand of the repolymerization reaction in AAS, resulting in a greater change in the content of bound water than that of M1 and M3.

It can be seen from Figure 9a that the variation trend of OH^-, Ca^{2+}, Al^{3+}, and Na^+ content in the pore solution with MK and alkali dosages was similar to the trend of water content between gel layers and TG mass loss, and the OH^- and Na^+ concentration decreased when the MK content increased. It indicates that the activator was gradually consumed by MK, and N−A−S−H gel was generated.[39,50] The chemically bound water of N−A−S−H gel was mainly attached to the Si/Al skeleton in the form of terminal hydroxyl groups,[50] and the bonding ability of the interlayer bound water was weaker, which led to the reduction of the bound water content in the TG analysis. When the alkali dosages increased, the OH^- and Na^+ concentration in the pore solution and the bound water content in the gel increased subsequently. Compared with M3 and E3, T3 specimens contained more gel bound water and the concentration of OH^- and Na^+ was close to that of sample M0, which indicated that there was a higher degree of reaction. After F−T cycles, the OH^- concentration in the pore solution decreased due to the induced depolymerization reaction and ion leaching caused by osmotic pressure.[41,59] The OH^- loss rates of M2 and E3 were 11.68 and 14.02%, respectively; the loss rate was higher than those of the other groups. Considering the changes of M2 and E3 bound water (see Figure 8a) and the weak binding ability of the bound water in the hybrid gel, it indicates that part of OH^- in the F−T process is consumed by further polymerization reaction, and the products fill the pores, which is interpreted as an enhancement of F−T resistance.

The concentrations of Ca^{2+} and Al^{3+} were higher in the pore solution due to the rapid dissolution of BFS in sample M0. With the increase of MK content, the Ca^{2+}, Al^{3+}, and Na^+ concentrations in the pore solution gradually decreased. With the increase of alkali dosage, the solubility of precursor increases and the ion concentration increases. In the F−T cycles, Ca^{2+} of the pore solution gradually leached out. The leaching rate of ions is the ratio of leaching ion concentration after F−T to the ion concentration before the F−T treatment. As shown in Figure 9b, the Ca^{2+} leaching rate of sample M0 was the highest, while sample M2 and E3 had lower Ca^{2+} leaching rates. It may be related to the water absorption rate in Figure 8b. The higher the water absorption, the higher the mass loss in the first region of TG, which leads to the enhancement of the weight loss peak at about 80 °C and the increase of Ca^{2+} leaching rate. The leaching rate of Al^{3+} was

https://doi.org/10.1021/acsomega.3c01600
ACS Omega 2023, 8, 20869−20880

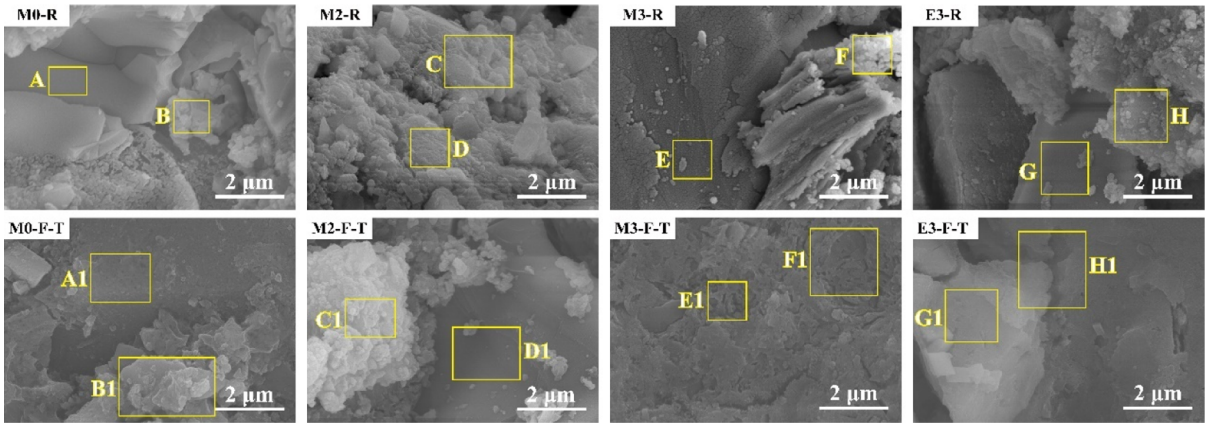

Figure 10. SEM images of the BFS/MK samples before F−T cycles.

Table 6. EDS Analysis of AAS (Elemental Atomic Percentage/%)

sample	EDS spots	Ca	Si	Al	Na	Ca/Si	Al/Si	Na/Si
M0-R	A	60.81	25.19	12.25	1.76	2.41	0.49	0.07
	B	48.92	26.96	13.32	10.80	1.81	0.49	0.40
M0-F−T	A1	36.19	33.26	11.00	19.55	1.09	0.33	0.59
	B1	51.56	31.12	13.36	3.96	1.65	0.43	0.13
M2-R	C	24.85	41.67	24.52	8.96	0.60	0.59	0.22
	D	27.92	38.56	18.83	14.69	0.72	0.49	0.38
M2-F−T	C1	18.87	32.31	34.33	14.49	0.58	1.06	0.45
	D1	19.86	36.84	31.05	12.25	0.54	0.84	0.33
M3-R	E	23.94	41.61	23.62	10.82	0.58	0.57	0.26
	F	17.37	44.46	25.99	12.18	0.39	0.58	0.27
M3-F−T	E1	16.61	44.47	25.59	13.33	0.36	0.60	0.30
	F1	16.01	45.42	26.64	11.93	0.35	0.59	0.26
E3-R	G	23.04	41.25	21.19	14.52	0.56	0.51	0.35
	H	31.74	41.20	20.49	6.56	0.77	0.50	0.16
E3-F−T	G1	25.84	39.32	20.92	13.92	0.66	0.53	0.35
	H1	20.48	42.38	21.84	15.30	0.48	0.52	0.36

similar to that of Ca^{2+}, with an average leaching rate of about 15%. According to the dotted line (average leaching rate) in Figure 9b, the order of the ion leaching rate in the F−T process is as follows: $Ca^{2+} > Al^{3+} > Na^{+} > OH^{-}$. Compared with sample M0, the incorporation of MK reduces the leaching of Ca^{2+} in the F−T process. The high alkali dosage increased Na^{+} and OH^{-} leaching in which Na^{+} has a high concentration and the leaching of Na^{+} has a large effect on the properties of the specimens. The low leaching rates of Na^{+} in the sample E3 and the high leaching rate of Ca^{2+}, Al^{3+}, and Na^{+} in sample M3 indicates that pores will affect ion leaching, which further leads to performance deterioration.

3.7. SEM−EDS Analysis and Gel Change. The micromorphology of samples with different MK incorporations and alkali dosages before and after F−T were analyzed, as shown in Figure 10. The slag was activated by silicate and sodium hydroxide, and the Ca−O bond and Al−O bond in the slag broke successively to produce free ions and finally bridged with silicate ions in the alkali activator to form C−S−H and C−A−S−H gels. Due to the short reaction time, the incompletely reacted slag was wrapped by the C−A−S−H gel,[60] and the gel was the main reaction product. When mixed with MK, MK needs to react with a large amount of activators to generate N−A−S−H gel, the hydration degree in AAS was weakened and less gel was formed, resulting in weaker binding.[33] In Figure 9, loose porous gel structures can be observed in the M3-R and M3-F−T samples. The gel modulus of sample E3 increased on the basis of M3 due to the increase of alkali dosages,[33] with a dense gel structure. The observed results were consistent with the development of compressive strength.

With the incorporation of MK, the Al/Si ratio increased and the Ca/Si ratio decreased slightly. Both Na and Si content increased when the alkali dosages increased. The gel products of M0 were mainly C−(A)−S−H with a high Ca/Si ratio. When the MK content continued to increase, gel products with the coexistence of C−A−S−H and N−A−S−H were generated. According to the Al/Si ratio of the samples obtained from the energy spectrum analysis in Table 6, the incorporation of MK increased the Al/Si ratio of the samples compared to sample M0. This can be attributed to the fast initial release rate of Al from MK, which reacts with silicate to form aluminosilicate oligomers.[38] When the content of MK increased, the available silicate in the precursor decreased, which resulted in lower compressive strength.[61] When the MK content was 30 wt %, the Na/Si ratio showed a slight increase with the increase of alkali dosages, and the relative content of aluminum and silicon decreased. The content of Na in the gels of E3 increased, mainly balancing the anion in the aluminum−oxygen tetrahedra.[62] Sample M3 formed more dispersed gels due to the excess of MK or activator and led to the presence of gel products of AAS wrapping MK or alkali particles, which was unfavorable to the development of strength.

https://doi.org/10.1021/acsomega.3c01600
ACS Omega 2023, 8, 20869−20880

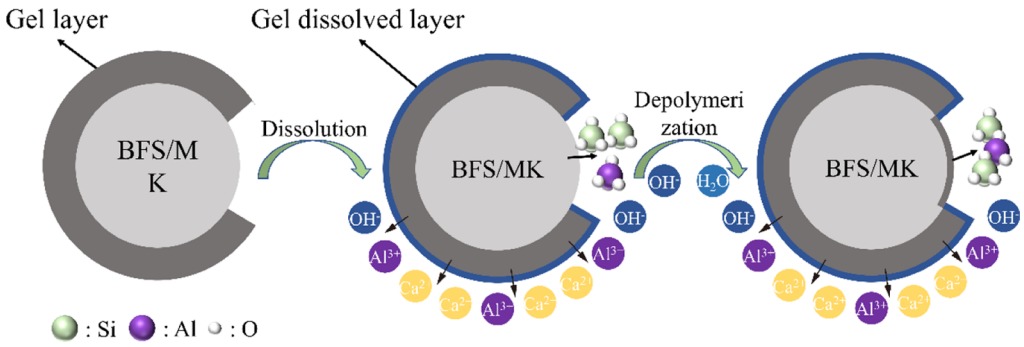

Figure 11. Schematic diagram of gel dissolution and depolymerization during F−T condition.

Table 6 shows the EDS analysis of AAS (atomic percentage of elements/%). Compared with the elemental data from the EDS analysis, it can be found that Ca/Si in gel products decreased with the increase of MK incorporation and increased with the increase of alkali dosage. The content of Ca elements in the gel structure of M0, M2, M3, and E3 decreased after 50 F−T cycles. This was mainly due to the dissolution of the C−A−S−H gel products during F−T processes. It was consistent with the trend of ion leaching in pore solution. The decrease of Al/Si ratio in the gels of M0 should be related to bound water content, the high content of bound water easily enhances Al migration.[58] The effect of mixing MK on Al elemental is not significant since both MK and BFS contain a high content of Al−O tetrahedra. The slight increase of Al/Si in the gel structure induced by F−T should be influenced by the gel dissolution and the decrease of Ca content. The results showed that when the amount of MK was 20−30% and the alkalinity was 6−8 wt %, alkali-activated BFS/MK could form a gel with good stability, which could effectively inhibit the gel dissolution and leaching of Ca, Al, and other elements under F−T conditions.

A schematic diagram of gel dissolution and depolymerization during F−T conditions is shown in Figure 11. In addition to the growth of microcracks during the F−T cycle, the gel products in the alkali-activated BFS/MK were subject to dissolution by F−T and water absorption. Leaching of ions into the thawed water forms a dissolved layer on the gel surface. Due to the incomplete reaction of alkali-activated BFS/MK, the increase of free water in the pores causes a repolymerization reaction on the surface of the unreacted precursor and consumes some of the OH^- during the F−T cycles. Due to the MK incorporation and alkali dosages, the degree of dissolution and the repolymerization reaction vary for each sample, thus leading to different magnitudes of change in bound water. The repolymerization reaction of the gel can inhibit the F−T deterioration to some extent.

4. CONCLUSIONS

In this study, the mechanical properties and microstructure of AAS with different alkali dosages and different MK content during 50 F−T cycles were studied. The following conclusions can be drawn from the experimental tests and characterization:

(1) After 50 F−T cycles, the compressive strength loss of M0 was 11.9%. The compressive strength losses of specimens M1, M2, and E3 incorporated with MK were 3.66, 3.3, and 0.58%, respectively. The MK incorporation in AAS resulted in the increase of mass loss, the mass loss rate, and the compressive strength after 28 days curing satisfied the linear decay relationship.

(2) Higher alkali dosages or higher MK incorporation will lead to the increase of macropores in the range of 50−200 nm and reduced F−T resistance. The F−T cycles decreased the capillary pores and increased the micropores of E3. The specific surface area increased from 18.724 to 25.968 m^2/g, and the cumulative pore volume increased from 0.085 to 0.107 m^2/g after F−T cycles. The specific surface area of sample M0 increased from 10.013 to 19.253 m^2/g, and the cumulative pore volume increased from 0.027 to 0.056 m^2/g. The pore structure variation of sample E3 is lower than that of sample M0.

(3) During the F−T cycles, owing to the osmotic pressure, some pores of the water−thawed samples were saturated with water absorption, and Ca^{2+}, Al^{3+}, OH^-, Na^+ leached out. The order of the leaching rate was $Ca^{2+} > Al^{3+} > Na^+ > OH^-$. The ion concentration decreased with the increase of MK incorporation and increased with the increase of alkali dosage. Appropriate MK incorporation and alkali dosage could reduce the content of pore solution and formed the C−A−S−H/N−A−S−H hybrid gel with a cross-linked structure, which could effectively inhibit the ion leaching and pore water absorption.

AUTHOR INFORMATION

Corresponding Author

Yan He − *School of Chemistry and Chemical Engineering and Guangxi Key Lab of Petrochemical Resource Processing and Process Intensification Technology, Guangxi University, Nanning 530004, P. R. China;* orcid.org/0009-0000-7642-0149; Email: hey2013@gxu.edu.cn

Authors

Yongheng Zhang − *School of Chemistry and Chemical Engineering and Guangxi Key Lab of Petrochemical Resource Processing and Process Intensification Technology, Guangxi University, Nanning 530004, P. R. China*

Xuemin Cui − *School of Chemistry and Chemical Engineering and Guangxi Key Lab of Petrochemical Resource Processing and Process Intensification Technology, Guangxi University, Nanning 530004, P. R. China;* orcid.org/0000-0003-1818-8470

Leping Liu − *College of Chemistry and Science, Guangxi Key Laboratory of Natural Polymer Chemistry and Physics, Nanning Normal University, Nanning 530001, PR China*

Complete contact information is available at:

https://doi.org/10.1021/acsomega.3c01600
ACS Omega 2023, 8, 20869−20880

https://pubs.acs.org/10.1021/acsomega.3c01600

Notes

The authors declare no competing financial interest.

■ ACKNOWLEDGMENTS

This work was supported by the National Natural Science Foundation of China (51962024 and 51772055) and Guangxi Scientific and Technological Development Projects (AC19050011).

■ REFERENCES

(1) Qin, Z.; Lai, Y.; Tian, Y.; Yu, F. Frost-heaving mechanical model for concrete face slabs of earthen dams in cold regions. *Cold Reg. Sci. Technol.* **2019**, *161*, 91−98.
(2) Teng, F.; Qiu, W.-L.; Pan, S.-S.; Hu, H.-s. Experimental study on seismic performance of precast segmental concrete columns after seawater freeze-thaw cycles. *Constr. Build. Mater.* **2020**, *260*, 120482.
(3) Mejdoub, R.; Hammi, H.; Khitouni, M.; Suñol, J. J.; M'Nif, A. The effect of prolonged mechanical activation duration on the reactivity of Portland cement: Effect of particle size and crystallinity changes. *Constr. Build. Mater.* **2017**, *152*, 1041−1050.
(4) Rovnaník, P.; Kusák, I.; Bayer, P.; Schmid, P.; Fiala, L. Comparison of electrical and self-sensing properties of Portland cement and alkali-activated slag mortars. *Cem. Concr. Res.* **2019**, *118*, 84−91.
(5) Wang, J.; Xu, H.; Xu, D.; Du, P.; Zhou, Z.; Yuan, L.; Cheng, X. Accelerated carbonation of hardened cement pastes: Influence of porosity. *Constr. Build. Mater.* **2019**, *225*, 159−169.
(6) Shuai, Q.; Xu, Z.; Yao, Z.; Chen, X.; Jiang, Z.; Peng, X.; An, R.; Li, Y.; Jiang, X.; Li, H. Fire resistance of phosphoric acid-based geopolymer foams fabricated from metakaolin and hydrogen peroxide. *Mater. Lett.* **2020**, *263*, 127228.
(7) Chen, S.; Zhang, Y.; Yan, D.; Jin, J.; Tian, Y.; Liu, Y.; Qian, X.; Peng, Y.; Fujitsu, S. The influence of Si/Al ratio on sulfate durability of metakaolin-based geopolymer. *Constr. Build. Mater.* **2020**, *265*, 120735.
(8) Toufigh, V.; Jafari, A. Developing a comprehensive prediction model for compressive strength of fly ash-based geopolymer concrete (FAGC). *Constr. Build. Mater.* **2021**, *277*, 122241.
(9) Khale, D.; Chaudhary, R. Mechanism of geopolymerization and factors influencing its development: a review. *J. Mater. Sci.* **2007**, *42*, 729−746.
(10) Tian, X.; Rao, F.; León-Patiño, C. A.; Song, S. Co-disposal of MSWI fly ash and spent caustic through alkaline-activation consolidation. *Cem. Concr. Compos.* **2021**, *116*, 103888.
(11) Yip, C. K.; Lukey, G. C.; van Deventer, J. S. J. The coexistence of geopolymeric gel and calcium silicate hydrate at the early stage of alkaline activation. *Cem. Concr. Res.* **2005**, *35*, 1688−1697.
(12) Li, Z.; Nedeljković, M.; Chen, B.; Ye, G. Mitigating the autogenous shrinkage of alkali-activated slag by metakaolin. *Cem. Concr. Res.* **2019**, *122*, 30−41.
(13) Chen, Z.; Ye, H. Improving sulphuric acid resistance of slag-based binders by magnesium-modified activator and metakaolin substitution. *Cem. Concr. Compos.* **2022**, *131*, 104605.
(14) Borges, P. H. R.; Banthia, N.; Alcamand, H. A.; Vasconcelos, W. L.; Nunes, E. H. M. Performance of blended metakaolin/blastfurnace slag alkali-activated mortars. *Cem. Concr. Compos.* **2016**, *71*, 42−52.
(15) Bernal, S. A. Effect of the activator dose on the compressive strength and accelerated carbonation resistance of alkali silicate-activated slag/metakaolin blended materials. *Constr. Build. Mater.* **2015**, *98*, 217−226.
(16) Zhao, M.; Zhang, G.; Htet, K. W.; Kwon, M.; Liu, C.; Xu, Y.; Tao, M. Freeze-thaw durability of red mud slurry-class F fly ash-based geopolymer: Effect of curing conditions. *Constr. Build. Mater.* **2019**, *215*, 381−390.
(17) Fu, Y.; Cai, L.; Yonggen, W. Freeze−thaw cycle test and damage mechanics models of alkali-activated slag concrete. *Constr. Build. Mater.* **2011**, *25*, 3144−3148.
(18) Setzer, M. J. Micro-Ice-Lens Formation in Porous Solid. *J. Colloid Interface Sci.* **2001**, *243*, 193−201.
(19) Aiken, T. A.; Kwasny, J.; Sha, W.; Tong, K. T. Mechanical and durability properties of alkali-activated fly ash concrete with increasing slag content. *Constr. Build. Mater.* **2021**, *301*, 124330.
(20) Xing, Z.; He, D.; Wang, H.; Ye, Z.; Yang, S. Study on soil mechanics and frost resistance of fly ash−metakaolin geopolymer. *Arabian J. Geosci.* **2020**, *13*, 963.
(21) El Moustapha, B.; Bonnet, S.; Khelidj, A.; Leklou, N.; Froelich, D.; Babah, I. A.; Charbuillet, C.; Khalifa, A. Compensation of the negative effects of micro-encapsulated phase change materials by incorporating metakaolin in geopolymers based on blast furnace slag. *Constr. Build. Mater.* **2022**, *314*, 125556.
(22) Xiang, J.; Liu, L.; He, Y.; Zhang, N.; Cui, X. Early mechanical properties and microstructural evolution of slag/metakaolin-based geopolymers exposed to karst water. *Cem. Concr. Compos.* **2019**, *99*, 140−150.
(23) Xiang, J.; He, Y.; Liu, L.; Zheng, H.; Cui, X. Exothermic behavior and drying shrinkage of alkali-activated slag concrete by low temperature-preparation method. *Constr. Build. Mater.* **2020**, *262*, 120056.
(24) Akçaözoğlu, S.; Ulu, C. Recycling of waste PET granules as aggregate in alkali-activated blast furnace slag/metakaolin blends. *Constr. Build. Mater.* **2014**, *58*, 31−37.
(25) Chinese National Standard. *Test Code for Hydraulic Concrete, SL 352-2006*; Ministry of Water Resources of the People's Republic of China: Beijing, China, 2006.
(26) Natkunarajah, K.; Masilamani, K.; Maheswaran, S.; Lothenbach, B.; Amarasinghe, D. A. S.; Attygalle, D. Analysis of the trend of pH changes of concrete pore solution during the hydration by various analytical methods. *Cem. Concr. Res.* **2022**, *156*, 106780.
(27) Sun, M.; Zou, C.; Xin, D. Pore structure evolution mechanism of cement mortar containing diatomite subjected to freeze-thaw cycles by multifractal analysis. *Cem. Concr. Compos.* **2020**, *114*, 103731.
(28) Na, S.; Zhang, W.; Taniguchi, M.; Quy, N. X.; Hama, Y. Experimental Investigation of Material Properties and Self-Healing Ability in A Blended Cement Mortar with Blast Furnace Slag. *Materials* **2020**, *13*, 2564.
(29) Kljajević, L. M.; Nenadović, S. S.; Nenadović, M. T.; Bundaleski, N. K.; Todorović, B. Ž.; Pavlović, V. B.; Rakočević, Z. L. Structural and chemical properties of thermally treated geopolymer samples. *Ceram. Int.* **2017**, *43*, 6700−6708.
(30) Marvila, M. T.; Azevedo, A. R. G.; Delaqua, G. C. G.; Mendes, B. C.; Pedroti, L. G.; Vieira, C. M. F. Performance of geopolymer tiles in high temperature and saturation conditions. *Constr. Build. Mater.* **2021**, *286*, 122994.
(31) Saludung, A.; Azeyanagi, T.; Ogawa, Y.; Kawai, K. Effect of silica fume on efflorescence formation and alkali leaching of alkali-activated slag. *J. Cleaner Prod.* **2021**, *315*, 128210.
(32) Ma, Y.; Hu, J.; Ye, G. The pore structure and permeability of alkali activated fly ash. *Fuel* **2013**, *104*, 771−780.
(33) Zhang, Z.; Li, L.; Ma, X.; Wang, H. Compositional, microstructural and mechanical properties of ambient condition cured alkali-activated cement. *Constr. Build. Mater.* **2016**, *113*, 237−245.
(34) Chousidis, N.; Ioannou, I.; Rakanta, E.; Koutsodontis, C.; Batis, G. Effect of fly ash chemical composition on the reinforcement corrosion, thermal diffusion and strength of blended cement concretes. *Constr. Build. Mater.* **2016**, *126*, 86−97.
(35) Liu, J.; Ou, G.; Qiu, Q.; Chen, X.; Hong, J.; Xing, F. Chloride transport and microstructure of concrete with/without fly ash under atmospheric chloride condition. *Constr. Build. Mater.* **2017**, *146*, 493−501.
(36) Kogbara, R. B.; Iyengar, S. R.; Grasley, Z. C.; Masad, E. A.; Zollinger, D. G. A review of concrete properties at cryogenic

temperatures: Towards direct LNG containment. *Constr. Build. Mater.* **2013**, *47*, 760−770.
(37) He, B.; Xie, M.; Jiang, Z.; Zhang, C.; Zhu, X. Temperature field distribution and microstructure of cement-based materials under cryogenic freeze-thaw cycles. *Constr. Build. Mater.* **2020**, *243*, 118256.
(38) Weng, L.; Sagoe-Crentsil, K. Dissolution processes, hydrolysis and condensation reactions during geopolymer synthesis: Part I—Low Si/Al ratio systems. *J. Mater. Sci.* **2007**, *42*, 2997−3006.
(39) Burciaga-Díaz, O.; Escalante-García, J. I. Structural transition to well-ordered phases of NaOH-activated slag-metakaolin cements aged by 6 years. *Cem. Concr. Res.* **2022**, *156*, 106791.
(40) Sun, G. K.; Young, J. F.; Kirkpatrick, R. J. The role of Al in C−S−H: NMR, XRD, and compositional results for precipitated samples. *Cem. Concr. Res.* **2006**, *36*, 18−29.
(41) Mollah, M. Y. A.; Yu, W.; Schennach, R.; Cocke, D. L. A Fourier transform infrared spectroscopic investigation of the early hydration of Portland cement and the influence of sodium lignosulfonate. *Cem. Concr. Res.* **2000**, *30*, 267−273.
(42) Garcia-Lodeiro, I.; Palomo, A.; Fernández-Jiménez, A.; Macphee, D. E. Compatibility studies between N-A-S-H and C-A-S-H gels. Study in the ternary diagram Na2O−CaO−Al2O3−SiO2−H2O. *Cem. Concr. Res.* **2011**, *41*, 923−931.
(43) Pouhet, R.; Cyr, M. Carbonation in the pore solution of metakaolin-based geopolymer. *Cem. Concr. Res.* **2016**, *88*, 227−235.
(44) Rovnaník, P. Effect of curing temperature on the development of hard structure of metakaolin-based geopolymer. *Constr. Build. Mater.* **2010**, *24*, 1176−1183.
(45) Dupuy, C.; Gharzouni, A.; Sobrados, I.; Tessier-Doyen, N.; Texier-Mandoki, N.; Bourbon, X.; Rossignol, S. Formulation of an alkali-activated grout based on Callovo-Oxfordian argillite for an application in geological radioactive waste disposal. *Constr. Build. Mater.* **2020**, *232*, 117170.
(46) Fernández-Jiménez, A.; Puertas, F.; Sobrados, I.; Sanz, J. Structure of Calcium Silicate Hydrates Formed in Alkaline-Activated Slag: Influence of the Type of Alkaline Activator. *J. Am. Ceram. Soc.* **2003**, *86*, 1389−1394.
(47) Roy, B. N. Infrared Spectroscopy of lead and Alkaline-Earth Aluminosilicate Glasses. *J. Am. Ceram. Soc.* **1990**, *73*, 846−855.
(48) Kapeluszna, E.; Kotwica, Ł.; Różycka, A.; Gołek, Ł. Incorporation of Al in C-A-S-H gels with various Ca/Si and Al/Si ratio: Microstructural and structural characteristics with DTA/TG, XRD, FTIR and TEM analysis. *Constr. Build. Mater.* **2017**, *155*, 643−653.
(49) Song, H.; Jeong, Y.; Bae, S.; Jun, Y.; Yoon, S.; Eun Oh, J. A study of thermal decomposition of phases in cementitious systems using HT-XRD and TG. *Constr. Build. Mater.* **2018**, *169*, 648−661.
(50) Morandeau, A.; Thiéry, M.; Dangla, P. Investigation of the carbonation mechanism of CH and C-S-H in terms of kinetics, microstructure changes and moisture properties. *Cem. Concr. Res.* **2014**, *56*, 153−170.
(51) Steiner, S.; Lothenbach, B.; Proske, T.; Borgschulte, A.; Winnefeld, F. Effect of relative humidity on the carbonation rate of portlandite, calcium silicate hydrates and ettringite. *Cem. Concr. Res.* **2020**, *135*, 106116.
(52) Prabahar, J.; Vafaei, B.; Ghahremaninezhad, A. The Effect of Hydrogels with Different Chemical Compositions on the Behavior of Alkali-Activated Slag Pastes. *Gels* **2022**, *8*, 731.
(53) Vafaei, B.; Farzanian, K.; Ghahremaninezhad, A. The influence of superabsorbent polymer on the properties of alkali-activated slag pastes. *Constr. Build. Mater.* **2020**, *236*, 117525.
(54) Prabahar, J.; Vafaei, B.; Baffoe, E.; Ghahremaninezhad, A. The Effect of Biochar on the Properties of Alkali-Activated Slag Pastes. *Construct. Mater.* **2021**, *2*, 1−14.
(55) Kamseu, E.; Cannio, M.; Obonyo, E. A.; Tobias, F.; Bignozzi, M. C.; Sglavo, V. M.; Leonelli, C. Metakaolin-based inorganic polymer composite: Effects of fine aggregate composition and structure on porosity evolution, microstructure and mechanical properties. *Cem. Concr. Compos.* **2014**, *53*, 258−269.
(56) Zhang, J.; Tan, H.; Cai, L.; He, X.; Yang, W.; Liu, X. Ultra-fine slag activated by sodium carbonate at ambient temperature. *Constr. Build. Mater.* **2020**, *264*, 120695.
(57) Zhu, X.; Qian, C.; He, B.; Chen, Q.; Jiang, Z. Experimental study on the stability of C-S-H nanostructures with varying bulk CaO/SiO2 ratios under cryogenic attack. *Cem. Concr. Res.* **2020**, *135*, 106114.
(58) Zhang, Y.; Zhang, J.; Jiang, J.; Hou, D.; Zhang, J. The effect of water molecules on the structure, dynamics, and mechanical properties of sodium aluminosilicate hydrate (NASH) gel: A molecular dynamics study. *Constr. Build. Mater.* **2018**, *193*, 491−500.
(59) Ren, J.; Lai, Y. Study on the durability and failure mechanism of concrete modified with nanoparticles and polypropylene fiber under freeze-thaw cycles and sulfate attack. *Cold Reg. Sci. Technol.* **2021**, *188*, 103301.
(60) Yang, J.; Li, D.; Fang, Y. Effect of synthetic CaO-Al2O3-SiO2-H2O on the early-stage performance of alkali-activated slag. *Constr. Build. Mater.* **2018**, *167*, 65−72.
(61) Rafeet, A.; Vinai, R.; Soutsos, M.; Sha, W. Effects of slag substitution on physical and mechanical properties of fly ash-based alkali activated binders (AABs). *Cem. Concr. Res.* **2019**, *122*, 118−135.
(62) Wan, H.; Yuan, L.; Zhang, Y. Insight Into the Leaching of Sodium Alumino-Silicate Hydrate (N-A-S-H) Gel: A Molecular Dynamics Study. *Front. Mater.* **2020**, *7*, 56.

https://doi.org/10.1021/acsomega.3c01600
ACS Omega 2023, 8, 20869−20880